Transnational University Limburg is a unique collaboration of two universities in two countries: the University of Hasselt and Maastricht University.

UHASSELT
KNOWLEDGE IN ACTION

www.uhasselt.be
Universiteit Hasselt
Campus Hasselt:
Martelarenlaan 42 | 3500 Hasselt
Campus Diepenbeek:
Agoralaan Gebouw D | 3590 Diepenbeek

UHASSELT
KNOWLEDGE IN ACTION

Maastricht University

Faculty of Medicine and Life Sciences
School for Life Sciences
Master of Biomedical Sciences

Master's thesis

Exploring Prussian Blue as a Safe-and-Sustainable-by-Design Cathode Material for Sodium-Ion Batteries

Reja Trippaers

Thesis presented in fulfillment of the requirements for the degree of Master of Biomedical Sciences, specialization Environmental Health Sciences

SUPERVISOR :
Prof. dr. An HARDY
Prof. dr. Nelly SAENEN

MENTOR :
Prof. dr. Karen SMEETS
dr. Dries DE SLOOVERE

2024
2025

Faculty of Medicine and Life Sciences
School for Life Sciences
Master of Biomedical Sciences

Master's thesis

Exploring Prussian Blue as a Safe-and-Sustainable-by-Design Cathode Material for Sodium-Ion Batteries

Reja Trippaers

Thesis presented in fulfillment of the requirements for the degree of Master of Biomedical Sciences, specialization Environmental Health Sciences

SUPERVISOR :

Prof. dr. An HARDY

Prof. dr. Nelly SAENEN

MENTOR :

Prof. dr. Karen SMEETS

dr. Dries DE SLOOVERE

Exploring Prussian Blue as a Safe-and-Sustainable-by-Design Cathode Material for Sodium-Ion Batteries

Reja Trippaers[1,2,3], Prof. Dr. Nelly Saenen[1], Dr. Ir. Dries De Sloovere[2,3], Prof. Dr. Karen Smeets[1], Prof. Dr. Marlies K. Van Bael[2,3] and Prof. Dr. An Hardy[2,3]

[1]Research Group Zoology: Biodiversity and Toxicology, Centre for Environmental Sciences (CMK), Universiteit Hasselt, Campus Diepenbeek, Agoralaan Building D-B-3590 Diepenbeek

[2] Design & Synthesis of INorganic materials for Energy applications , Institute for Material Research (IMO-IMOMEC), Universiteit Hasselt, Campus Diepenbeek, Wetenschapspark 1, 3590 Diepenbeek

[3]EnergyVille, Thor Park 8320, 3600 Genk

*Running title: *Safe-by-Design Prussian Blue for SIB Cathodes*

To whom correspondence should be addressed: Nelly Saenen, Tel: +32 (11) 26 83 30; Email: nelly.saenen@uhasselt.be or An Hardy, Tel: +32 (11) 26 83 08; Email: an.hardy@ uhasselt.be

Keywords: Prussian blue particles, Sodium-ion battery cathodes, Rate capability testing, Cytotoxicity assessment, Dental pulp stem cells

ABSTRACT

The growing demand for sustainable and safe energy storage solutions has accelerated research into sodium-ion batteries as an alternative to lithium-ion systems. Prussian blue analogues have emerged as promising cathode materials due to their low cost, environmental friendliness, biocompatibility, and favorable electrochemical properties. However, to ensure the safety of these materials, especially for vulnerable populations, it is essential to evaluate their potential toxicity alongside their electrochemical performance during the design and testing phases. Thirteen different Prussian blue particle samples were synthesized by a precipitation approach, systematically varying parameters such as flow rate, temperature, atmosphere, and the presence of chelating ligands. These materials were characterized using a comprehensive set of physicochemical techniques to determine particle size, crystal structure, water content, and Fe(II)/Fe(III) ratio. A subset of samples was then used for parallel testing of (i) electrochemical performance through rate capability testing, and (ii) toxicity via cell viability assays on dental pulp stem cells. The results suggest that maintaining a low Fe(II)/Fe(III) ratio helps reduce cytotoxic effects. Smaller particle size enhances electrochemical performance, although excessively small particles may increase toxicity. Additionally, higher crystallinity improves electrochemical performance. Therefore, balancing particle size and Fe(II)/Fe(III) ratio, alongside achieving good crystallinity, is crucial for developing Prussian blue cathode materials that combine high battery performance with minimal cytotoxicity. Optimizing this balance can guide the safe-by-design development of Prussian blue-based cathodes for sodium-ion batteries.

INTRODUCTION

The world is currently undergoing a significant energy transition, with a global shift from conventional fossil fuels to renewable, green energy sources. However, green energy, such as wind and solar power, is intermittent and only available at certain times. As a result, the demand for efficient energy storage solutions is expected to rise dramatically in the coming years (1). One of the most convenient ways to store energy is through rechargeable batteries, which can be widely used in applications ranging from small portable devices to electric vehicles and large-scale energy storage systems (2).

Among rechargeable batteries, lithium-ion technology stands out for its high energy density, fast charge and discharge rates, stable performance, and relatively simple manufacturing process compared to other battery types (3). As a result, it is expected to become the dominant energy storage technology (3). However, the growing demand for lithium is expected to drive up its price and put pressure on supplies, as lithium is not abundantly available in nature (1). The EU estimates that lithium demand could rise 18-fold by 2030 and 60-fold by 2050 compared to 2020 (3). Moreover, projections indicate that by 2029, the lithium supply will no longer be able to meet this rapidly growing demand (4). In addition to lithium, other key battery cathode materials, such as cobalt, nickel, and manganese, are also classified as critical raw materials by the EU, highlighting the challenge of securing a stable supply (5).

Beyond resource scarcity, lithium-ion batteries pose significant environmental and social concerns. The extraction of their raw materials contributes to water and air pollution, land degradation, biodiversity loss, and hazardous waste generation (6). Social issues include human rights violations, such as forced child labor in cobalt mining, and conflicts over water resources and land use linked to lithium extraction (6, 7). Additionally, lithium-ion battery disposal remains a major challenge. Currently, only about 5% of lithium-ion batteries are recycled globally (8). Since recycling remains costly and underdeveloped, most batteries continue to end up in landfills. Many of them contain toxic heavy metals like cobalt and nickel in their cathodes. As these batteries corrode, these harmful chemicals leach into the soil and water, contaminating ecosystems. Additionally, these batteries are prone to causing landfill fires, releasing harmful gasses and fine particulate matter into the atmosphere. These airborne toxins can settle on surfaces or be inhaled directly, posing further health risks (9). Toxic metals from lithium-ion batteries are known to disrupt the structure of carbohydrates, lipids, proteins, and enzymes. Exposure through polluted crops, fruits, or airborne dust has been linked to genetic damage and lower academic performance in children (9). Moreover, these metals are often released as nanoparticles, which are more bioavailable and can easily penetrate biological barriers. Studies have shown that such nanoparticles induce oxidative stress, DNA damage, and impaired cell function, raising concerns about their long-term health effects (9).

Currently, efforts are being made to improve recycling rates and develop more efficient recycling methods. These improvements could help reduce the release of toxic heavy metals into the environment and provide a more secure, circular source of lithium. However, such measures alone are insufficient to meet the rapidly growing demand for energy storage (3). Therefore, there is an urgent need for a sustainable alternative that relies on abundant, non-toxic materials and addresses both environmental and social concerns.

One such alternative is sodium-ion technology, which has gained increasing attention due to its sustainability potential. Sodium is the fourth most abundant element on earth and is widely distributed, making it a more stable and cost-effective option than lithium (1). Additionally, sodium can be sourced from saltwater, reducing the environmental impact of mining. Sodium-ion batteries are also considered safer due to their better thermal stability, which lowers the risk of fire (2). Despite these advantages, sodium-ion batteries are still less developed than lithium-ion batteries. Their lower energy density, shorter lifespan, and slower charging speed make them less suitable for applications where size and weight are critical, such as high-performance electric vehicles and portable electronics. However, ongoing research continues to improve their performance, and scientists are confident that sodium-ion

batteries can replace some lithium-ion batteries, particularly in applications where energy density is less crucial, such as affordable electric cars with shorter ranges or large-scale stationary energy storage (2, 10). Furthermore, the components and the electrical storage mechanisms of sodium-ion batteries are quite similar to those of lithium-ion batteries, making the transition between the two technologies feasible (1).

To fully realize the potential of a well-performing, more sustainable, and affordable battery, selecting the right cathode (i.e. positive electrode) is crucial. Prussian blue analogues are among the most promising options, as they combine sustainability with strong electrochemical performance. They are made from abundant, non-toxic elements using a simple, low-cost, and scalable co-precipitation method (11). In addition to their environmental benefits, these materials also exhibit favorable structural and electrochemical properties. Prussian blue analogues offer high theoretical energy density and a stable three-dimensional framework structure (12). They are represented by the structural formula $A_xP[R(CN)_6]\cdot wH_2O$, where A is an insertion ion (sodium in the case of sodium-ion batteries), and P and R are transition metals. Together, these atoms form a rigid open framework with large spaces where sodium ions can easily move in and out **(Figure 1a)** (10). Additionally, Prussian blue analogues offer a high theoretical specific capacity of 170 mA g^{-1} (based on $Na_2Fe[Fe(CN)_6]$) because of a theoretical two-electron redox reaction **(Figure 1c)** (10).

While Prussian blue is generally considered non-toxic, it is often applied as nanoparticles in batteries. As with many engineered nanomaterials, further research is needed to confirm their safety, particularly regarding any potential health risks for vulnerable populations, such as pregnant women and their unborn children (14). If these nanoparticles are released into the environment during the manufacturing, use, or disposal of sodium-ion batteries, pregnant women may be exposed. Nanoparticles are particles that occur at the nanometer scale (1-100 nm) and exhibit unique properties due to their small size and high surface area (15). These characteristics make them highly effective in applications like sodium-ion batteries, but they also heighten potential toxicity. Smaller particles generally improve battery efficiency due to their larger surface area and shorter diffusion paths, which reduce mass transfer limitations and enable faster charge/discharge rates. However, this increased surface area also makes the nanoparticles more reactive, potentially causing unwanted side reactions between the cathode and electrolyte. These reactions can lead to issues such as self-discharge, poor cycle stability, and reduced calendar life (16).

Furthermore, they also tend to be more toxic, as their smaller size enables easier penetration into cells, while the increased surface area leads to greater interaction with cellular components, potentially causing cellular damage (17). For example, Prussian blue nanoparticles have electron-accepting and donating properties that can possibly interfere with mitochondrial function in cells by interacting with the electron-transporting components of the respiratory chain. Such interactions can disrupt the generation of membrane potential, which is crucial for ATP production (15). Since

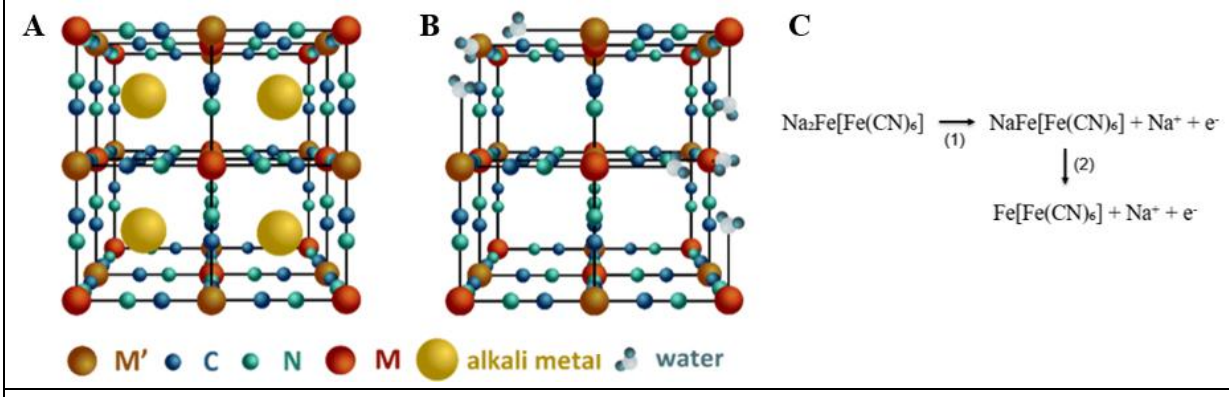

Fig.1 – (A) Ideal structure of Prussian blue containing alkali metals in the interstitial sites. **(B)** Partially defective Prussian blue structure, with water molecules occupying the defect sites (13). **(C)** Theoretical two-step redox reaction of Prussian Blue.

mitochondria are essential for energy production, especially during energy-intensive stages like early developmental processes, such interference could disrupt normal growth and developmental processes (18). Additionally, studies indicate that iron-based nanoparticles can induce toxicity mainly through the production of reactive oxygen species. This can lead to damage to genetic material or disruption of intracellular signaling, potentially reducing cell viability and inducing programmed cell death (19). Thus, while Prussian blue analogues show promise in sodium-ion batteries, further research is needed to balance their performance with safe-by-design considerations.

A good starting point to investigate developmental toxicity is *in vitro* through the use of dental pulp stem cells. These mesenchymal stem cells can effectively serve as a proxy for early developmental processes due to their ability to self-renew and differentiate into multiple tissue types, which mirrors some of the key characteristics of cells during early development (20). Additionally, they are more easily accessible and have a higher proliferation rate compared to bone marrow mesenchymal stem cells, making them ideal for high-throughput toxicity screening (21). On the other hand, compared to *in vivo* studies or the use of embryonic or induced pluripotent stem cells, this approach is faster, less expensive, and avoids ethical concerns, while maintaining biological relevance (20).

The primary goal of this research was to design Prussian blue particles ($Na_2Fe[Fe(CN)_6]$) for sodium-ion battery cathodes that minimize stem cell toxicity while maximizing battery performance. To achieve this, a variety of nano-, submicron-, and micron- sized particles were synthesized and their physicochemical properties were characterized using various methods. A selection of particles were incorporated into sodium-ion batteries to evaluate their electrochemical performance through rate capability tests. Toxicity was assessed by examining their effects on cell viability and the expression of genes related to oxidative stress, apoptosis and mitochondrial dynamics. Ultimately, this research aimed to advance sustainable battery technology that minimizes health risks, addressing the growing demand for energy storage solutions while ensuring the safety of future generations.

EXPERIMENTAL PROCEDURES

Prussian blue synthesis

Prussian blue particles were synthesized via coprecipitation by adding 25 mL sodium hexacyanoferrate(II) ($Na_4Fe(CN)_6$) and 25 mL iron(II) sulfate ($FeSO_4$) into a vessel containing water, following the method outlined by Kjeldgaard et al. (11). The Atlas HD Potassium reactor and Atlas XL Syringe Pump (Syrris Ltd, Royston, UK) were used to control temperature and flow rate. The solution was continuously stirred at 200 rpm. After synthesis, the mixture was aged for four hours, either entirely at room temperature or for 2 hours at 70 °C followed by 2 hours at room temperature. Parameters like temperature, flow rate, water volume, and aging were varied **(Table 1).** In synthesis 8 and 11 sodium citrate ($Na_3C_6H_5O_7$) was added to the $FeSO_4$ solution. In synthesis 9 and 12, sodium chloride (NaCl) was added to the water, and in synthesis 10 and 13, both $Na_3C_6H_5O_7$ and NaCl were added. Syntheses 11-13 were performed under a nitrogen atmosphere to prevent oxidation. After aging, the particles were filtered using a Büchner funnel with a 100 nm pore filter, washed with 50 mL water, and dried overnight at 60 °C.

Physicochemical characterization

Hydrodynamic particle size distributions were measured using dynamic light scattering (DLS). A 10 mg/mL stock suspension was prepared in Milli-Q water, sonicated for 10 minutes, and then diluted to 0.1 mg/mL prior to analysis. Measurements were performed using the Zeta PALS Zeta Potential Analyzer (Brookhaven Instruments Corporation, Nashua, USA) with the Particle Sizing software. Particle morphology and size were further investigated using transmission electron microscopy (TEM). Pioloform coated copper mesh grids were pre-treated with Alcian Blue before drop-casting a diluted nanoparticle suspension. Imaging was performed on a JEM-1400 Flash TEM (JEOL, Japan), equipped with a 20 MP XAROSA CMOS camera (EMSIS, Germany). Thermal stability and water content was determined by TGA (TA instruments Q600). The samples (~5 mg) were heated from room temperature to 400 °C at 10 °C/min under dry air atmosphere. The crystalline structure was determined by X-ray diffraction (XRD) using a Bruker D8

diffractometer equipped with a Cu Kα radiation source. Raman spectra were collected (Renishaw InVia Qontor Confocal Raman Microscope, 50x objective lens, 532 nm excitation wavelength [100 mW]) at room temperature. The Raman shift scale was calibrated using silicon. The measurements were performed in a continuous scan mode (exposure time of 5 s, 1% laser power, and a 2400 L mm^{-1} grating). For ICP-OES (Optima 3300 DV, PerkinElmer) analysis, samples were dissolved in a mixture of HCl, HNO_3, and HF (6:1:3), heated to 200°C for 15 minutes, and filtered prior to measurement.

Electrochemical characterization

Prussian blue particle samples 3, 9, 10, 11 and 13 were incorporated into coin cells to evaluate their electrochemical performance. Slurries with a total weight of 0.5 g dry matter were prepared, consisting of 85 wt% active material (Prussian blue), 10 wt% carbon black, and 5 wt% polyvinylidene fluoride (PVDF) in N-methylpyrrolidone (NMP). The amount of NMP required depended on the particle size. For samples 3 and 9, 2.5 g of NMP was used, while for samples 10, 11, 13, and the commercial variant, 1.875 g of NMP was added. The slurry was ball-milled (Retsch Emax) at 500 rpm for 30 minutes, then evenly spread onto 15 µm thick aluminum foil, forming a wet film with a thickness of 100 µm, and dried at 110 °C. Circular electrodes with a diameter of 15 mm were punched from the coated foil. The electrodes, along with the other battery components, were vacuum-dried overnight at 110 °C to remove any residual solvents. Half cells were assembled in an argon-filled glovebox using sodium metal as the counter and reference electrode. A 19 mm glass fiber separator (EL-CELL) was soaked with 120 µL of a 1 M $NaClO_4$ solution in a 1:1 (v/v) mixture of ethylene carbonate (EC) and propylene carbonate (PC) as the electrolyte. The assembled cells were evaluated for their electrochemical performance through rate capability tests, where the cells were cycled between 2.2 and 4 V vs Na^+/Na at C-rates of 0.1, 0.2, 0.5, 1, and 2 C, each for 5 cycles, followed by an additional 5 cycles at 0.1 C.

Dental pulp stem cell cultivation

Human dental pulp stem cells were provided by the Biomedical Research Institute at Hasselt University and cultured in vented 25 cm^2 cell culture flasks using α-Minimum Essential Medium (α-MEM; VWR, Radnor, USA), supplemented with 10% fetal bovine serum (FBS; Sigma-Aldrich, St. Louis, USA), 1% l-glutamine (VWR, Radnor, USA), and 1% penicillin-streptomycin (Gibco, Thermo Fisher Scientific, Waltham, USA). Cells were maintained in an incubator at 37 °C with 5% CO_2 and high humidity. The medium was refreshed twice a week, and cultures were passaged at 70-80% confluence using 0.05% trypsin (Gibco, Thermo Fisher Scientific, Waltham, USA), incubated for 5 minutes. Cells with passage numbers below 10 were used to prevent cellular changes and ensure consistency between experiments.

Particle Preparation for Cell Experiments

A stock suspension of 5 mg/mL (for cell viability experiments) and 1 mg/mL (for qPCR experiments) was prepared in pre-filtered and autoclaved Milli-Q water, and sonicated for 10 minutes in a water bath sonicator at room temperature. The particle suspensions were subsequently diluted to the desired concentrations in complete cell growth medium prior to exposure to the cells.

Assessment of cell viability

The impact on cell viability was assessed for Prussian blue particle samples 3, 4, 6, 8, 9, 10, 11, 12, and 13 using a combination of two non-invasive fluorescent indicator dyes: Alamar Blue, which measures metabolic activity, and 5-Carboxyfluorescein Diacetate Acetoxymethyl Ester (CFDA-AM), which evaluates the combination of metabolic activity and membrane integrity. 2,000 cells were seeded in 96-well plates and grown until they reached 50-70% confluence, ensuring that they were in the proliferative stage. The cells were then exposed for 24 hours to a wide concentration range of Prussian blue particle dilutions (1, 50, 100, 250, and 500 µg/mL). These relatively high concentrations were chosen as a range-finding experiment to identify at which levels cytotoxic effects begin to appear. After exposure, the medium was removed, and the cells were

washed twice with 150 µL of sterile PBS (VWR, Radnor, USA). Next, 120 µL of a working solution containing 5 % Alamar Blue (Thermo Fisher Scientific, Waltham, USA) and 0.1 % CFDA-AM (Thermo Fisher Scientific, Waltham, USA) was added to each well and incubated for 30 minutes in the dark. Fluorescence of Alamar Blue (excitation 530/25 nm, emission 595/35 nm) and CFDA-AM (excitation 485/20 nm, emission 528/20 nm) was then measured using a fluorescence plate reader (Fluostar Omega, BMG Labtech, Champigny-sur-Marne, France). To check for possible optical interference, all Prussian blue dilutions were added to wells without cells and underwent the same experimental procedure.

Measurement of gene expression

To evaluate the expression of genes related to oxidative stress, apoptosis, and mitochondrial dynamics **(Table 2)**, RT-qPCR was performed using Prussian blue particle samples 3, 9, and 11. A total of 30,000 cells were seeded in 12-well plates and cultured until they reached 50-70% confluence. The cells were then exposed to Prussian blue nanoparticle suspensions at concentrations of 0.1, 1, and 100 µg/mL for 24 hours. After exposure, the medium was removed and the cells were washed twice with 1 mL of warm dPBS (Gibco, Thermo Fisher Scientific, Waltham, USA). Subsequently, 350 µL of RTL lysis buffer (QIAGEN, Hilden, Germany), supplemented with 10 µL/mL beta mercaptoethanol (Sigma-Aldrich, St. Louis, USA), was added to each well. The lysates were immediately frozen at -80 °C. Total RNA was isolated using phenol-chloroform extraction. RNA purity (260/280 and 260/230 absorbance ratios) and concentration (absorbance at 260 nm) were measured using a Nanodrop spectrophotometer (ND-1000, Fisher Scientific, Brussels, Belgium). Samples with a 260/230 ratio below 1.5 were diluted to 50 µL and re-purified using phenol-chloroform extraction. Afterwards, only samples with a 260/230 ratio above 1.5 and a concentration greater than 25 ng/µL were included for further analysis. Turbo DNase treatment (Turbo DNA-free Kit, Invitrogen, Fisher Scientific, Brussels, Belgium) was performed to remove residual DNA. RNA was reverse transcribed into cDNA using the GoScript Reverse Transcriptase system (Promega, Wisconsin, US), following the manufacturer's protocol. Gene expression was quantified using the QuantStudio 5 RT-qPCR system (Applied Biosystems, Fisher Scientific, Brussels, Belgium) in a 384-well format. Each reaction consisted of 5 µL of Fast SYBR Green PCR Master Mix (Applied Biosystems), 0.3 µL of forward and reverse primers, 1.9 µL RNAse-free water, and 2.5 µL of cDNA (10 ng/µL). The thermal cycling conditions were as follows: 95 °C for 20 s, followed by 40 cycles of 95 °C for 1 s and 60 °C for 20 s. Relative gene expression was calculated using the $2^{-\Delta\Delta Ct}$ method, normalized

Table 2 – Selection of genes and primer information

Gene	Name	Forward primer (5'-3')	Reverse primer (5'-3')
Oxidative stress related genes			
SOD1	Superoxide dismutase 1	TGCAGGTCCTCACTTTAATCCTC	AGTCTCCAACATGCCTCTCTTC
SOD2	Superoxide dismutase 2	AGCCCAGATAGCTCTTCAGC	CCAGCAACTCCCCTTTGGG
CAT	Catalase	AGCTTAGCGTTCATCCGTGT	GCCACTAGCTTGCATTTG
GPX1	Glutathione peroxidase 1	TCCGGGACTACACCCAGATG	TCTTGGCGTTCTCCTGATGC
GPX4	Glutathione peroxidase 4	GCCTTCCCGTGTAACCAGTT	TTCATCCACTTCCACAGCGG
HMOX1	Heme oxygenase 1	CTGCTCAACATCCAGCTCTTTG	CTCCACGGGGGCAGAATCTT
Apoptosis related genes			
P53	Tumor protein p53	CTTCCCTGGATTGGCAGC	TTTCAGGAAGTAGTTTCCATAGGT
Bax	Bcl-2 associated X protein	GGGCCCACCAGCTCTGA	CCTGCTCGATCCTGGATGA
BCL2	B-cell lymphoma 2	TTGTGGCCTTCTTTGAGTTCGGTG	GGTGCCGGTTCAGGTACTCAGTCA
Mitochondrial dynamics related genes			
MFN1	Mitofusin 1	CTGCCTCCTCTCCGCCTTTA	TCGCCTTCTTAGCCAGCACA
MFF	Mitochondrial fission factor	TTTCCTTCTCCCACTGCTGC	TTTCTGGGACCCTCATTCGC
Reference genes			
RPLP0	Ribosomal Protein Lateral Stalk Subunit P0	CGTCCTCGTGGAAGTGACAT	TAGTTGGACTTCCAGGTCGC
TBP	TATA-Box Binding Protein	CCGCCGGCTGTTTAACTTC	AGAAACAGTGATGCTGGGTCA
UBC	Ubiquitin C	CAGCCGGGATTTGGGTCG	CACGAAGATCTGCATTGTCAAGT
GAPDH	Glyceraldehyde-3-Phosphate Dehydrogenase	TGTTCGTCATGGGTGTGAAC	ATGGCATGGACTGTGGTCAT

to four reference genes that were selected based on expression stability using geNorm in qBase **(Table 2)**.

Statistical Analysis and data visualization

All statistical analyses were performed using RStudio (version 4.2.2). Normality and homoscedasticity were assessed using the Shapiro-Wilk and Levene's tests, respectively. If the assumptions were met, a one-way ANOVA was conducted, followed by Dunnett's post hoc test to determine significant differences between the control and treatment groups. If the assumptions of normality and homoscedasticity were not satisfied, log or square root transformations were applied. When these transformations failed to normalize the data, a non-parametric Kruskal-Wallis test was performed, followed by Dunn's post hoc test with false discovery rate (FDR) correction. A p-value < 0.05 was considered statistically significant. Figures were created using Origin 2025 (OriginLab Corporation) and Microsoft PowerPoint. TEM image analysis was performed using FIJI (ImageJ 1.45p).

RESULTS AND DISCUSSION

Physicochemical characterization

Thirteen different Prussian blue particle samples were prepared by varying precipitation synthesis parameters such as flow rate, temperature, atmosphere, and the presence of chelating ligands **(Table 1)**. These are referred to as PB-1 through PB-13 throughout the text. This set of materials was subjected to a comprehensive series of physicochemical characterization techniques.

First, particle size was assessed using DLS **(Figure S1)**. The synthesized Prussian blue particles exhibited a bimodal size distribution, which likely corresponds to the size of primary particles and their aggregates or agglomerates. Primary particle sizes varied between 17 nm and 700 nm (hydrodynamic diameter), with a few particles reaching sizes of several micrometers. Particle size was strongly influenced by synthesis parameters. Lowering the flow rate or increasing the water volume in the reactor vessel led to lower reagent concentrations, resulting in slower nucleation and the formation of fewer nuclei. This led to the formation of larger particles, as more material was available per nucleus. Increasing the temperature to 70 °C resulted in smaller particles, since higher temperatures promote nucleation **(Figure 2A, left)** (22). Adding sodium citrate increased particle size, as it forms complexes with metal ions, causing the latter to react more slowly with hexacyanoferrate, delaying nucleation and allowing more time for particle growth (11). Combining sodium citrate with sodium chloride led to an even larger particle size, possibly due to enhanced aggregation driven by increased ionic strength. Interestingly, sodium chloride alone resulted in smaller particles. This may be because sodium chloride increases the ionic strength of the solution, reducing electrostatic repulsion between precursor ions and facilitating nucleation **(Figure 2A, right)**. However, the specific mechanism of salt-mediated nucleation in this system is not well described in the literature, so the exact explanation remains unclear. Finally, synthesizing under a nitrogen atmosphere had a limited effect in the presence of sodium chloride. However, nitrogen atmosphere synthesis involving sodium citrate produced large particles that were no longer measurable by DLS, likely due to reduced oxidation of Fe(II) to Fe(III), which slows nucleation (23).

TEM analysis was performed on Prussian blue particle samples PB-3, PB-9, and PB-11 to further investigate particle morphology **(Figure 2B)**. These particle samples were selected because they are the focus of detailed toxicity tests presented later in this thesis. The images revealed that most particles had a cubic shape, likely reflecting the cubic crystal lattice of Prussian blue, which can promote relatively uniform growth in all directions. Based on a qualitative analysis (n = 10 particles per sample), PB-3 had a particle size of 25 nm (mean MinFeret), PB-9 of 42 nm, and PB-11 mainly consisted of particles larger than the DLS detection limit, around 1.9 µm. In PB-9, in addition to the larger primary particles, many very small, spherical nanoparticles (~8 nm) were observed near the edges of larger structures, which could indicate fragmentation or detachment.

Table 1 – Overview table of synthesis parameters and physicochemical/electrochemical characteristics

PB-Sample	Synthesis parameters							Physicochemical and electrochemical characteristics				
	Reagents	**Conc**	**Volume water**	**Flow rate**	**Temp**	**Aging**	**Atm**	**Hydrodynamic diameter**	**Crystallite size**	**Na/Fe**	**Weight loss at 390°C**	**Capacity at 2C**
1	$Na_4Fe(CN)_6$ $FeSO_4$	0.1 M 0.1 M	/	Manual slow drip	RT	10 min	/	17 nm	22.3 nm	-	42%	-
2	$Na_4Fe(CN)_6$ $FeSO_4$	0.1 M 0.1 M	50 ml	4 ml/min	RT	4h	/	84 nm	25.4 nm	-	34%	-
3	$Na_4Fe(CN)_6$ $FeSO_4$	0.1 M 0.1 M	50 ml	1 ml/min	RT	4h	/	122 nm	26.8 nm	0.27	33%	67 mAh g^{-1}
4	$Na_4Fe(CN)_6$ $FeSO_4$	0.1 M 0.1 M	100 ml	0.5 ml/min	RT	4h	/	131 nm	26.9 nm	-	36%	-
5	$Na_4Fe(CN)_6$ $FeSO_4$	0.1 M 0.1 M	200 ml	1 ml/min	70°C RT	2h 2h	/	108 nm	-	-	29%	-
6	$Na_4Fe(CN)_6$ $FeSO_4$	0.1 M 0.1 M	200 ml	0.5 ml/min	70°C RT	2h 2h	/	101 nm	46.2 nm	-	29%	-
7	$Na_4Fe(CN)_6$ $FeSO_4$	0.1 M 0.1 M	200 ml	1 ml/min	RT	4h	/	157 nm	34.5 nm	-	32%	-
8	$Na_4Fe(CN)_6$ $FeSO_4$ $Na_3C_6H_5O_7$	0.1 M 0.1 M 1.0 M	200 ml	1 ml/min	70°C RT	2h 2h	/	234 nm	62.3 nm	-	16%	-
9	$Na_4Fe(CN)_6$ $FeSO_4$ NaCl	0.1 M 0.1 M 2.5 M	200 ml	1 ml/min	70°C RT	2h 2h	/	107 nm	48.1 nm	0.45	24%	83 mAh g^{-1}
10	$Na_4Fe(CN)_6$ $FeSO_4$ $Na_3C_6H_5O_7$ NaCl	0.1 M 0.1 M 1.0 M 2.5 M	200 ml	1 ml/min	70°C RT	2h 2h	/	685 nm	63.3 nm	0.89	11%	0 mAh g^{-1}
11	$Na_4Fe(CN)_6$ $FeSO_4$ $Na_3C_6H_5O_7$	0.1 M 0.1 M 1.0 M	200 ml	1 ml/min	70°C RT	2h 2h	N_2	-	61.1 nm	0.80	18%	2 mAh g^{-1}
12	$Na_4Fe(CN)_6$ $FeSO_4$ NaCl	0.1 M 0.1 M 2.5 M	200 ml	1 ml/min	70°C RT	2h 2h	N_2	106 nm	47.8 nm	-	19%	-
13	$Na_4Fe(CN)_6$ $FeSO_4$ $Na_3C_6H_5O_7$ NaCl	0.1 M 0.1 M 1.0 M 2.5 M	200 ml	1 ml/min	70°C RT	2h 2h	N_2	-	47.2 nm	1.04	13%	21 mAh g^{-1}

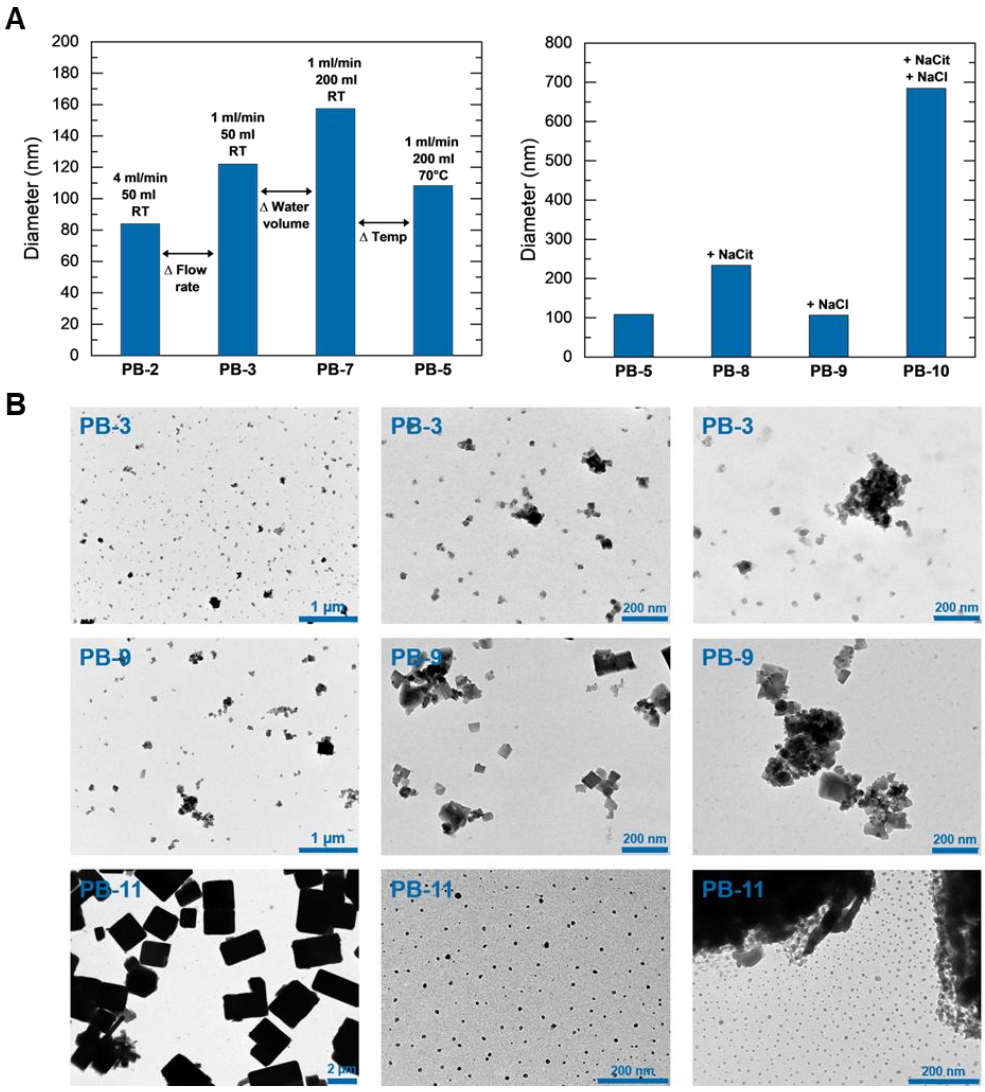

Fig. 2 – (A) Effect of varying synthesis parameters on the hydrodynamic diameter of the primary particles. (B) TEM images of PB-3, PB-9, and PB-11 acquired at different magnifications. For PB-3 and PB-9: 10k, 40k and 40k; for PB-11: 2.5k, 60k and 60k.

The crystal structure of the particles was investigated using XRD **(Figure 3A)**. PB-8 to PB-13 displayed sharper peaks with a higher signal-to-noise ratio compared to PB-1 to PB-7, indicating improved crystallinity, likely due to increased crystallite size and fewer lattice vacancies (23, 24). The crystallite size was estimated from the full width at half maximum (FWHM) of the most intense peak (2θ ~17°) using the Scherrer equation: $D = k\lambda/(\beta \cos\theta)$, where D is the average crystallite size, k is the Scherrer constant (0.89), λ is the wavelength (Cu Kα = 0.15406 nm), β is the FWHM, and θ is the Bragg angle **(Figure 3B)**. Crystallite sizes ranged from 22 to 64 nm, and like the hydrodynamic diameter, were influenced by synthesis parameters. The crystallite size of PB-5 was excluded from interpretation, as this diffractogram was recorded after the sample was ball-milled, a process that can alter crystallite size. By comparing PB-2, PB-3, and PB-7, it can be observed that lowering the flow rate or increasing the water volume in the reactor vessel led to larger crystallites, a trend that mirrors their hydrodynamic diameters **(Table 1)**. Similarly, the addition of sodium citrate, alone or in combination with sodium chloride, also increased crystallite size, consistent with their effect on hydrodynamic diameter. Although the effect of temperature and sodium chloride alone could not be assessed due to the unreliability of the crystallite size of PB-5, one or both of these parameters should

have contributed to the larger crystallite size observed in PB-9 compared to PB-7 **(Table 1)**.

Furthermore, a systematic shift of diffraction peaks toward lower 2θ values was observed in PB-8 to PB-13. The magnitude of this shift, based on the most intense peak (2θ ~ 17°), increases in the order: PB-9 (Δ2θ = 0.18°) < PB-12 (0.34°) < PB-8 (0.38°) < PB-10 (0.48°) < PB-11 (0.50°) < PB-13 (0.54°). According to Bragg's law ($n\lambda = 2d \sin\theta$), a decrease in 2θ corresponds to an increase in interplanar spacing. This shift is likely caused by the incorporation of a higher number of sodium ions, which expand the lattice in the cubic phase (23). These results suggest a relative increase in sodium content across the samples in the following order: PB-1 to PB-7 < PB-9 < PB-12 < PB-8 < PB-10 < PB-11 < PB-13. This trend implies that sodium content is influenced by the addition of sodium citrate, sodium chloride, and the nitrogen atmosphere, with sodium citrate having the strongest effect, followed by the nitrogen atmosphere, while sodium chloride alone has only a minor effect.

Furthermore, PB-1 to PB-9 and PB-12 exhibited diffraction patterns consistent with the reference pattern of cubic Prussian blue, confirming a cubic crystal structure. In contrast, PB-10, PB-11, and PB-13 displayed peak splitting that deviates from the cubic symmetry. According to literature, this suggests a phase transition to either a rhombohedral or monoclinic structure (23, 25). Visually, the diffraction pattern matches most closely with rhombohedral Prussian blue analogues reported in the literature. However, Rietveld refinement would be needed to confirm the exact crystal structure. Both rhombohedral and monoclinic phases have been associated with higher sodium content in the structure. This correlates well with the observed peak shifts, which suggest that PB-10, PB-11, and PB-13 exhibit the highest sodium incorporation.

These findings are further supported by Raman analyses, focusing on the C≡N stretching region **(Figure 3C)**. PB-3, PB-6, and PB-9 display similar peak positions, with their rightmost peak located at a Raman shift of 2152 cm^{-1}. In PB-12, this peak is slightly shifted to a lower wavenumber of 2144 cm^{-1}. Finally, PB-10, PB-11, and PB-13 show similar spectra, but with the rightmost peak further shifted to 2132 cm^{-1}. Cyanide ligands coordinated to Fe(II) typically relate to lower Raman shifts compared to those coordinated to Fe(III) (23, 26). These data confirm this trend, with PB-10, PB-11, and PB-13 exhibiting the lowest Raman shifts, followed by PB-12, and then PB-3, PB-6, and PB-9. This pattern indicates a higher Fe(II) content compared to Fe(III), which corresponds to increased sodium incorporation in these samples to maintain charge neutrality. Finally, these results are confirmed by ICP-OES analysis, which quantitatively confirms the trend in sodium incorporation. The Na/Fe ratios increase progressively from PB-3 (0.27) to PB-9 (0.45), PB-11 (0.80), PB-10 (0.89), and PB-13 (1.04). Due to time and resource constraints, not all samples could be further analyzed using Raman spectroscopy and ICP-OES. However, we ensured that all particle samples incorporated into battery coin cells were fully characterized by these techniques.

Finally, TGA was performed to investigate the water content and thermal stability of the Prussian blue particle samples **(Figure 4)**. PB-1 to PB-7 exhibited two distinct weight loss regions: the first occurred from room temperature up to approximately 150-180 °C, with samples synthesized at room temperature losing between 20-22% of their weight, and samples made at 70 °C losing about 18%. This loss likely corresponds to the evaporation of adsorbed and interstitial water (23). The second weight loss region began around 220 °C and continued at higher temperatures, initially due to the loss of coordinated water, and later likely due to the release of gases such as hydrogen cyanide, cyanogen, and carbon dioxide resulting from the thermal decomposition of Prussian blue (23, 27, 28). In contrast, PB-9 and PB-12 displayed an almost linear weight loss profile without clearly separated zones, with no distinct separation between the evaporation of interstitial water, the loss of coordinated water, and the onset of structural decomposition. Lastly, PB-8, PB-10, PB-11, and PB-13 showed a single major weight loss event between approximately 180 and 240 °C. Samples made with both sodium citrate and sodium chloride lost approximately 11% of their weight, while those made with only sodium citrate lost around 15%. After this temperature range, the weight of PB-8 and PB-10 stabilized, showing minimal further weight loss up to 400 °C, whereas PB-11 and PB-13 continued to degrade slowly. This

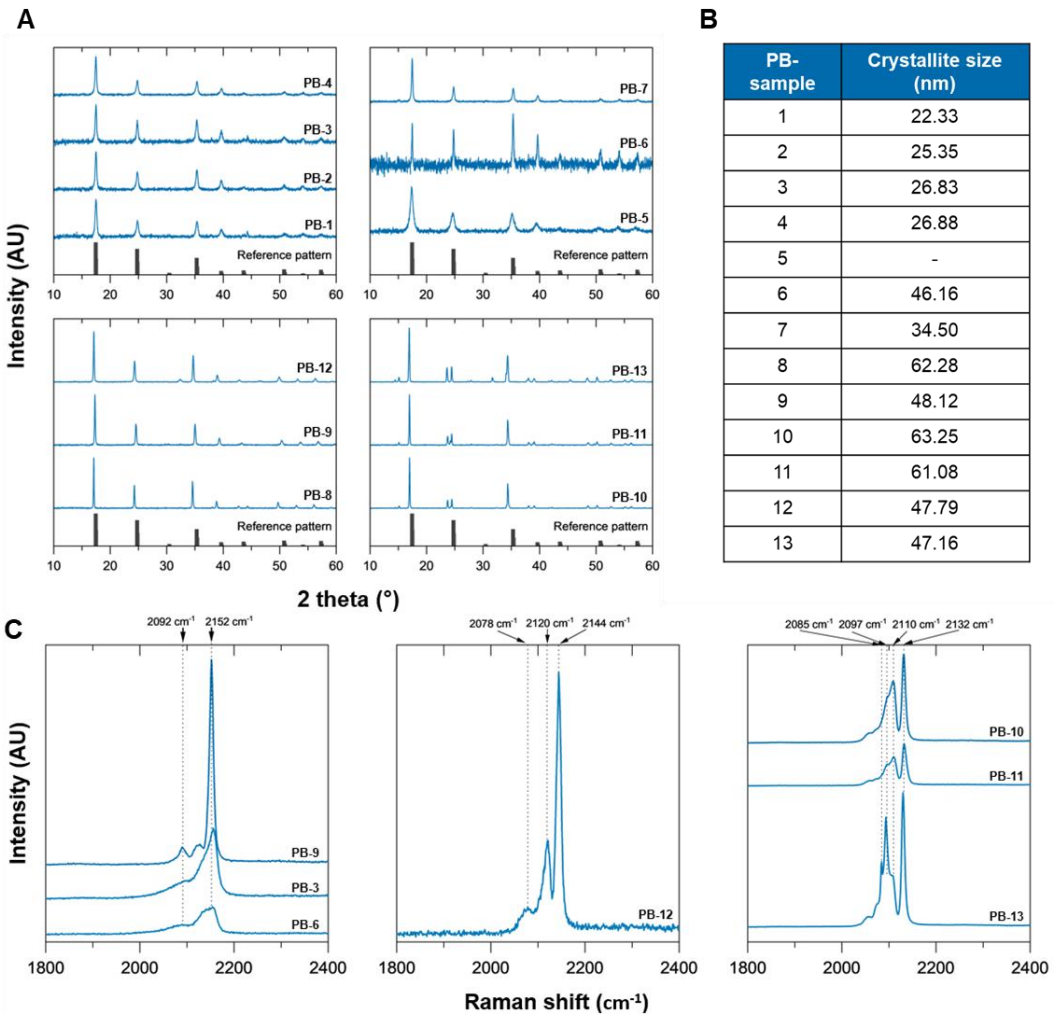

PB-sample	Crystallite size (nm)
1	22.33
2	25.35
3	26.83
4	26.88
5	-
6	46.16
7	34.50
8	62.28
9	48.12
10	63.25
11	61.08
12	47.79
13	47.16

Fig. 3 – (A) Normalized X-ray diffraction (XRD) patterns of the synthesized samples. All patterns were normalized to the intensity of the first diffraction peak. The reference pattern (bottom) corresponds to the expected cubic Prussian blue structure. (B) Average crystallite size calculated using the Scherrer equation from the most intense peak. (C) Raman spectra showing the characteristic C≡N stretching vibrations, with specific peak positions indicated above the spectra.

main weight loss step was likely associated with the loss of coordinated water. Due to overlapping weight loss steps, it is difficult to precisely quantify the water content in the particles. However, the data suggest that synthesis at 70 °C reduces water content compared to synthesis at room temperature. The addition of sodium chloride and sodium citrate, especially in combination, further decreases water content with the combination yielding particles with the lowest water content. Notably, particles synthesized with sodium citrate under ambient conditions appear thermally stable up to 400 °C. Furthermore, when linking these findings to other physicochemical characteristics, it appears that particles with larger crystallite sizes and higher sodium content generally contained less water.

Electrochemical characterization

To evaluate the electrochemical performance of the synthesized Prussian blue particles, a subset of samples was incorporated into half-cell coin cells and subjected to a rate capability test **(Figure 5A)**. These samples were selected to represent a broad range of physicochemical characteristics, allowing us to explore how variations in these properties affect performance. PB-3 was chosen for its small particle size, low crystallinity, low sodium content, and high water content. PB-9 also has

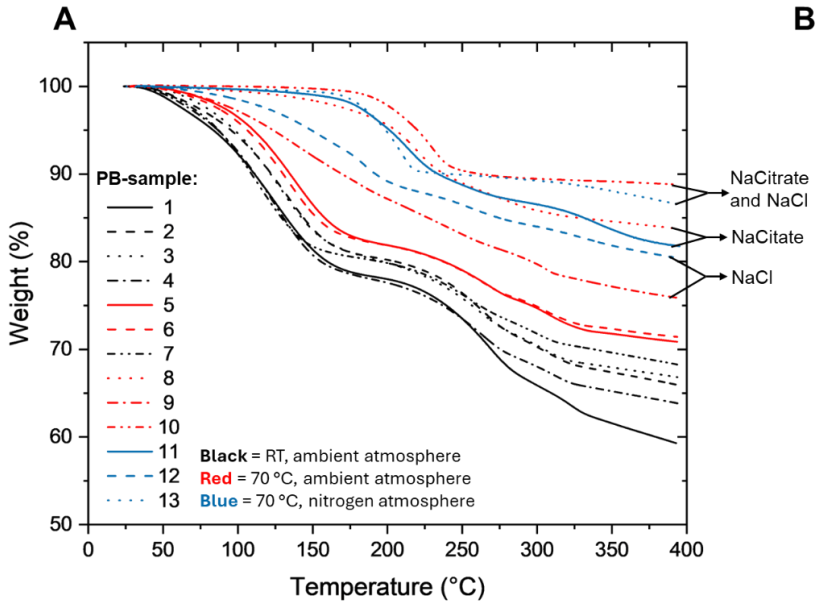

PB-sample	% weight loss
1	41
2	34
3	33
4	36
5	29
6	29
7	32
8	16
9	24
10	11
11	18
12	19
13	13

Fig. 4 – (A) Thermogravimetric analysis (TGA) curves showing weight (%) as a function of temperature. (B) Percentage weight loss at 390 °C for each sample.

small particles but differs from PB-3 by having a higher crystallinity and an intermediate water content. PB-10 consists of medium-sized particles with high crystallinity, high sodium content, and low water content. PB-11 and PB-13 were selected for their large particle sizes, high crystallinity, high sodium content, and low water content, however, PB-13 differs from PB-11 in having a smaller crystallite size **(Table 1)**.

PB-3 and PB-9 showed the highest specific discharge capacities of 67 mAh g^{-1} and 83 mAh g^{-1} at 2 C, respectively. PB-10, PB-11, and PB-13 displayed lower capacities across all C-rates, with PB-13 performing best among them. Interestingly, PB-10 outperformed PB-11 at low rates (<0.2 C), whereas the opposite was observed at higher rates. All samples nearly recovered their initial capacities when the C-rate was lowered again to 0.1 C, indicating good stability. PB-3 and PB-9 had similar but smaller particle sizes compared to the other samples, which likely contributed to their improved high-rate performance by reducing ion diffusion distances, thereby enhancing mass transfer and facilitating faster charge/discharge kinetics (16). This effect is especially important under high-rate conditions, where rapid ion and electron transport is essential to maintain capacity. Additionally, the combination of small particle size and higher crystallinity in PB-9 likely contributed to its superior rate performance compared to PB-3.

To better understand the electrochemical behavior, the galvanostatic charge-discharge profiles were examined **(Figure 5B)**. For PB-9, two distinct plateaus were observed: a high-voltage plateau around 3.40 V vs Na^+/Na and a low-voltage plateau around 2.28 V vs Na^+/Na. These correspond to the redox reactions of the two different iron sites in the Prussian blue structure ($Na_2Fe[Fe(CN)_6]$): Fe coordinated to nitrogen atoms at higher voltage, and Fe coordinated to carbon atoms at lower voltage **(Figure 1C)** (29). The discharge profile of PB-3 appeared more sloped, lacking well-defined plateau regions, which may be attributed to its lower crystallinity. PB-10, PB-11, and PB-13 displayed only the low-voltage plateau, indicating sodium-ion storage limited to Fe coordinated to carbon. The underlying reason for this limited redox activity is not entirely clear. However, these samples were found to contain very little water. Previous studies on metal-organic coordination compounds have shown that coordinated water can activate otherwise inert C=N sodium-storage sites and lower the energy barrier for sodium-ion insertion (30). This suggests that in our Prussian blue samples with low water content, some C≡N sites may remain inactive, restricting sodium storage to only part of the structure.

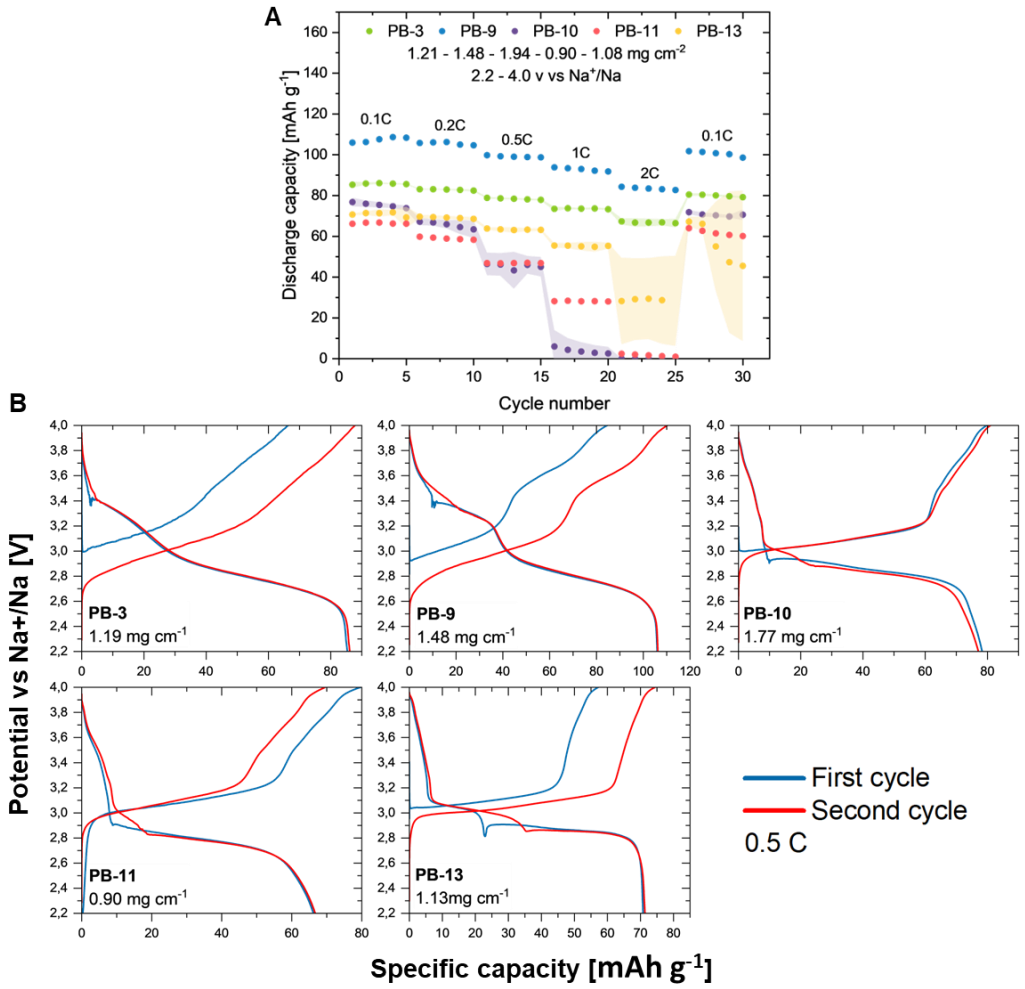

Fig. 5 – (A) Rate capability test at various current densities (C-rates). Shaded areas represent the standard deviation from replicate measurements: n = 3 for PB-3 and PB-13, and n = 2 for PB-10. For the remaining samples, only one coin cell showed reliable performance, so no standard deviation is shown. (B) Galvanostatic charge-discharge profiles from the first two cycles. The applied voltage window, C-rates, and electrode mass loadings are indicated in the corresponding figure.

Toxicity assessment

To assess the toxicity of the synthesized Prussian blue particles, a subset of samples was subjected to cell viability testing. As with the electrochemical tests, the selected samples represent a broad range of physicochemical characteristics. However, because it was feasible to include more samples in this assay, the original selection was expanded to ensure representation of all key synthesis groups. PB-3, PB-4, and PB-6 were synthesized without the use of a chelating agent, with PB-3 and PB-4 at synthesized room temperature, and PB-6 at 70 °C. PB-8, PB-9, and PB-10 were synthesized in the presence of sodium chloride, sodium citrate, and a combination of both, respectively. PB-11, PB-12, and PB-13 were synthesized under identical conditions as PB-8 to PB-10, but under a nitrogen atmosphere instead of ambient air **(Table 1)**. For all Prussian blue particle samples, a dose-dependent decrease in fluorescence was observed, indicating reduced cell viability at higher concentrations. The data are presented as both blank-corrected (accounting for background signal from assay reagents only) and interference-corrected (also accounting for any signal coming from the nanoparticles themselves processed through the same assay protocol). The Wilcoxon signed-rank test for paired data showed a statistically significant difference between the blank-corrected and interference-corrected viability values for nearly all particle and concentration

combinations in both assays. This shows that the Prussian blue particles interfere with the assay signals. However, when visually examining the pooled data from the CFDA-AM assay, the blank- and interference-corrected results mostly showed similar trends, with only some deviations at higher concentrations and a stronger decrease in viability for PB-12 and PB-13.

In contrast, the Alamar Blue assay showed more pronounced differences between blank- and interference-corrected data. For example, in PB-4 and PB-9, the concentration-dependent effect leveled off after interference correction, and for PB-11, the trend was even reversed. This suggests that the nanoparticles cause complex forms of interference. Several mechanisms may contribute to this. First, Prussian blue exhibits a broad absorption band in the visible spectrum, starting around 500 nm and peaking near 700 nm (31). This overlaps with both the excitation (560 nm) and emission (590 nm) wavelengths of Alamar Blue, which can interfere with the readout signal in several ways. Prussian blue may absorb part of the excitation light, reducing the energy available to excite the fluorophore, or it may absorb emitted fluorescence before it reaches the detector. Additionally, Prussian blue particles may quench the fluorescent signal, or cause light scattering that distorts the measurement. All these effects can lead to reduced signal intensity and, consequently, an overestimation of toxicity (32). Secondly, Alamar Blue relies on the metabolic activity of viable cells to reduce resazurin to fluorescent resorufin. However, Prussian Blue is redox-active and could potentially reduce resazurin independently of cellular metabolism, increasing the signal and causing an underestimation of toxicity (32). To fully understand and quantify these interferences, additional experiments are required. However, the interference appears too complex to be mitigated by merely introducing an additional correction. As a result, the interpretation of the Alamar Blue assay is less reliable in this context. Therefore, we primarily focused our interpretation on the interference-corrected CFDA-AM results.

Based on these results, PB-3 showed no significant decrease in cell viability at concentrations up to 100 µg/mL. Similarly, PB-4, PB-6, and PB-8 did not show significant differences compared to the untreated control at concentrations up to 50 µg/mL. For PB-9 and PB-10, a concentration of 1 µg/mL also did not cause significant reductions in viability. However, PB-11, PB-12, and PB-13 showed a significant decrease in cell viability at all tested concentrations. According to commonly used thresholds in the literature, cell viability values below 80% of untreated controls indicate cytotoxic effects. PB-3, PB-4, and PB-8 remained above this 80% threshold at concentrations up to 100 µg/mL, while PB-9 and PB-10 approached this threshold at the same concentrations. In contrast, PB-11, PB-12, and PB-13 consistently stayed below 80% across all concentrations, suggesting a higher cytotoxic potential.

The differences in cell viability seem to be influenced by two main particle characteristics: the Fe(II)/Fe(III) ratio and particle size. Studies show that Fe(II) reduces cell viability more strongly than Fe(III), likely because Fe(II) can directly participate in the Fenton reaction, producing a high number of free radicals (33). These radicals can cause direct injury to proteins, lipids, and nucleic acids, which can ultimately lead to detrimental effects such as lipid peroxidation damaging cellular membranes, mitochondrial dysfunction, activation of cell stress pathways, and ultimately cell death (34). In this study, particles with the lowest Fe(II)/Fe(III) ratio (PB-3, PB-4, and PB-6) also showed the lowest cytotoxicity among all samples. PB-9 and PB-12 have similar particle sizes but differ in Fe(II) content, PB-9 contains more Fe(II) than the least toxic particles, and PB-12 has even higher Fe(II) levels. Correspondingly, PB-9 exhibited increased toxicity compared to the least toxic particle samples, while PB-12 was even more toxic. PB-8 has a higher Fe(II)/Fe(III) ratio than PB-12 but is less toxic, which is likely due to its larger size. Larger particles have a smaller specific surface area relative to their volume, resulting in less surface available to interact with cellular components. Additionally, their larger size makes cellular uptake more difficult (17). PB-10, PB-11, and PB-13 have the highest Fe(II)/Fe(III) ratios among all tested particles and show the highest cytotoxicity, with PB-11 and PB-13 being even more toxic than PB-10. This is somewhat counterintuitive since PB-11 and PB-13 consist of the largest particles. However, TEM images suggest that small

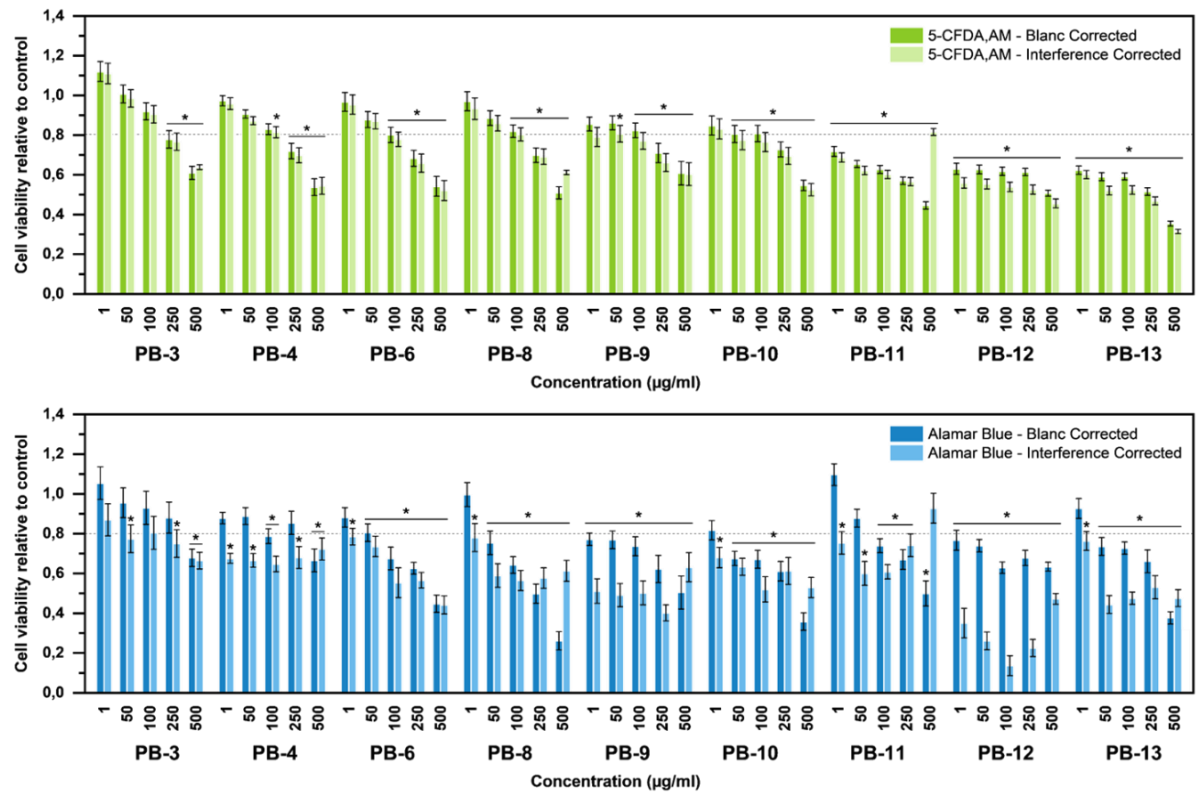

Fig. 6 – Cell viability (fold change relative to control) of dental pulp stem cells after 24 h exposure to various concentrations of Prussian blue particle suspensions, measured using 5-CFDA,AM (top) and Alamar Blue (bottom). Data are presented as mean ± standard error. Each concentration was tested in three independent experiments with three technical replicates per sample for PB-3 to PB-10, and in four independent experiments with three technical replicates for PB-11 to PB-13. Asterisks (*) indicate statistically significant differences compared to controls ($P < 0.05$), as determined by a non-parametric Kruskal-Wallis test followed by Dunn's post hoc test with FDR correction. The horizontal dotted line indicates the 80% cell viability threshold.

fragments may be released from these particles, which could potentially explain the increased toxicity **(Figure 2)**.

To further investigate the mechanisms underlying the observed toxicity differences, PB-3, PB-9, and PB-11 were selected. Dental pulp stem cells were exposed to 0.1, 1, and 100 µg/mL of these Prussian blue particle suspensions for 24 hours, after which gene expression changes related to oxidative stress, apoptosis, and mitochondrial dynamics were measured by qPCR **(Figure 7)**. The intermediate concentration of 1 µg/mL was chosen because most particles did not induce significant cytotoxicity at this level, enabling the assessment of sub-lethal cellular stress responses. The highest concentration of 100 µg/mL was selected as it approaches the cytotoxicity threshold for most samples, providing insight into gene expression changes under (near-)cytotoxic conditions. In addition, a lower concentration of 0.1 µg/mL was included to reflect a more realistic environmental exposure scenario. Although actual environmental levels of Prussian blue particles are difficult to estimate, studies on other engineered nanoparticles suggest that real-life exposures likely remain well below this value (35). The particle selection aimed to include samples with contrasting toxicological and electrochemical profiles. PB-3 was chosen due to its low toxicity and good electrochemical performance; PB-9 for its excellent battery performance, despite showing some toxicity at higher concentrations; and PB-11 as a highly toxic sample with distinct physicochemical properties. Among these, PB-3 has the lowest Fe(II)/Fe(III) ratio, followed by PB-9, with PB-

11 having the highest. This trend aligns with their cytotoxic potential. As previously discussed, Fe(II) is thought to contribute to toxicity by triggering oxidative stress via the Fenton reaction, leading to cellular damage such as lipid peroxidation, mitochondrial dysfunction, and apoptosis. To investigate whether these mechanisms underlie the observed toxicity differences, we selected qPCR markers targeting genes involved in oxidative stress response, cell death, and mitochondrial dynamics. This approach allows us to assess whether the trends observed in cell viability are reflected at the gene expression level.

Most genes showed no statistically or biologically relevant differences compared to the control. Gene expression changes are generally considered biologically relevant when they exceed a two-fold difference. However, even though some genes showed changes above this threshold, these were often not statistically significant. This is likely due to substantial variability in the data. The particle suspensions were unstable, which may have led to inconsistent exposure. In addition, natural biological variability between cells and, in some cases, a limited number of replicates likely contributed to the variation observed in the results. The most striking finding was that, for all particle samples, exposure to 100 µg/mL led to a more than two-fold increase in *HMOX1* gene expression. HMOX1 is known for its rapid upregulation in response to oxidative stress (36), suggesting that at this concentration, all particles likely trigger oxidative stress. This strong upregulation aligns with existing literature, where HMOX1 is frequently reported as the most responsive oxidative stress marker (37, 38). In PB-3, this change was accompanied by a more than two-fold decrease in *SOD1*, which has also been linked to oxidative stress in multiple studies (39, 40). Additionally, a more than two-fold change in *MFF* was observed for PB-3 at 1 µg/mL and PB-9 at 100 µg/mL, and in *MFN1* at 100 µg/mL. MFF promotes mitochondrial fission, while MFN1 facilitates mitochondrial fusion. Fusion helps mitigate cellular stress by allowing partially damaged mitochondria to merge and share their contents, which can help maintain mitochondrial function. Fission, on the other hand, enables the removal of damaged mitochondria and may promote apoptosis under severe stress conditions (41). The upregulation of these genes may indicate a shift in mitochondrial dynamics triggered by particle-induced stress. Since this effect was observed only for PB-3 and PB-9, which are significantly smaller than PB-11, it suggests that only the smaller particles can exert their toxicity through intracellular mechanisms involving the mitochondria. In contrast, PB-11 may not be efficiently taken up by the cells and could therefore exert its toxicity primarily at the cell surface level.

Interestingly, at the concentrations where cytotoxicity was observed for PB-9 and PB-11 in the viability assay, no changes were detected in the expression of pro- or anti-apoptotic genes, nor in oxidative stress-related genes other than *HMOX1*. Moreover, the extent of *HMOX1* upregulation did not correlate with Fe(II) content. This lack of consistent gene expression patterns aligned with cytotoxicity suggests that other cellular mechanisms beyond Fe(II)-mediated oxidative stress contribute to toxicity. While these findings do not provide further insight into the exact mechanisms underlying the observed toxicity, they also do not exclude the involvement of specific pathways. It is important to note that qPCR captures gene expression at a single time point, so effects may have already passed or not yet occurred. Furthermore, gene expression is measured only in the surviving cell population, which may have adapted or recovered from the initial stress. And finally, gene expression is an indirect measure of protein activity, it does not account for post-translational modifications, which can significantly influence protein function and cellular responses.

To gain more insight into the underlying toxicity mechanisms, additional experiments are needed. For instance, the qPCR analysis could be complemented with multiple timepoints to better capture dynamic gene expression changes. Alternatively, protein-level measurements using Western blotting could provide a more direct indication of protein expression and allow for the investigation of proteins that are regulated post-transcriptionally, which cannot be assessed through qPCR analyses. Furthermore, it would be valuable to support the gene expression data with live-cell fluorescence-based assays. These could include measurements of reactive oxygen

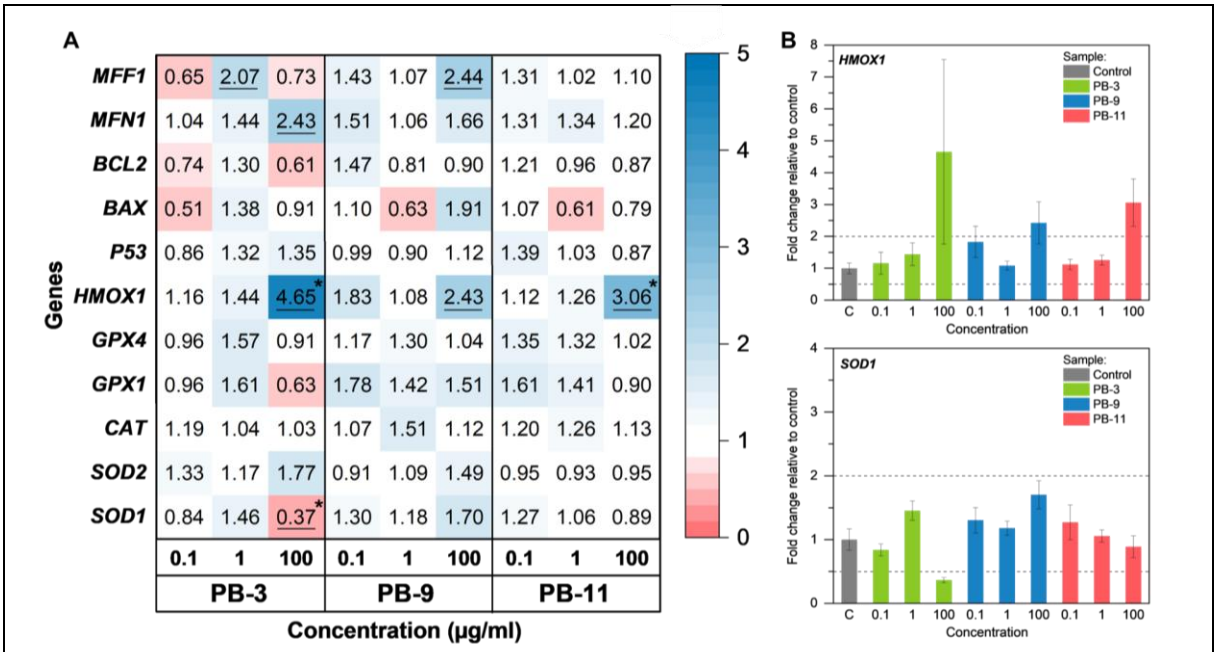

Fig. 7 – (A) Heatmap showing the fold change in gene expression relative to the untreated control. Data represent 3 to 7 replicates across two independent experiments. Asterisks (*) indicate statistically significant differences compared to controls ($P < 0.05$), determined using either a one-way ANOVA followed by Dunnett's post hoc test, or a non-parametric Kruskal-Wallis test followed by Dunn's post hoc test with FDR correction, depending on data distribution. A line under a value indicates a more than two-fold change in gene expression. (B) Fold change in gene expression of *HMOX1* and *SOD1*, shown as mean ± standard error.

species and mitochondrial membrane potential to evaluate oxidative stress and mitochondrial health more directly. However, before these assays can be applied, it is essential to evaluate possible interference between the particles and the fluorescent dyes. This step is crucial to determine whether these assays are suitable and, if so, which correction factors should be applied to ensure reliable interpretation of the results.

CONCLUSION

This research aimed to design Prussian blue particles for sodium-ion battery cathodes that minimize stem cell toxicity while maximizing battery performance. It provided valuable insights into how synthesis parameters influence the physicochemical characteristics of Prussian blue particles, and how these characteristics, in turn, affect both the electrochemical performance of batteries and toxicity towards dental pulp stem cells **(Table 3)**.

By systematically varying synthesis conditions, promising candidates were identified that combine high battery performance with minimal cytotoxicity. Two of the smallest synthesized Prussian blue samples (PB-3 and PB-9), with a relatively low Fe(II)/Fe(III) ratios, showed the highest specific discharge capacities of 67 mAh g^{-1} and 83 mAh g^{-1} at 2 C, respectively. PB-3 showed no signs of cytotoxicity at tested concentrations of 1, 50, and 100 µg/mL, maintaining cell viability above 80%. In contrast, PB-9, which had a slightly higher Fe(II)/Fe(III) ratio and greater crystallinity, hovered around the cytotoxicity threshold at these concentrations. These findings suggest that maintaining a low Fe(II)/Fe(III) ratio helps reduce cytotoxic effects. At the same time, smaller particle size enhances electrochemical performance, although excessively small particles can increase toxicity. Additionally, higher crystallinity improves electrochemical performance. Therefore, balancing particle size and Fe(II)/Fe(III) ratio, along with achieving good crystallinity, is crucial for developing Prussian blue cathode materials that deliver both high battery performance and minimal cytotoxicity.

Table 3 – Summery of the influence of synthesis parameters on physicochemical properties and their effect on capacity

Effect of synthesis parameters on physicochemical characteristics					
Diameter	Flow rate	-	**Na/Fe**	Flow rate	?
	Temperature	-		Temperature	?
	Volume water	+		Volume water	?
	Nitrogen atmosphere	+		Nitrogen atmosphere	+
	Sodium citrate	+		Sodium citrate	+
	Sodium chloride	~		Sodium chloride	+
	Sodium citrate + Sodium chloride	+		Sodium citrate + Sodium chloride	+
Crystallite size	Flow rate	-	**Weight loss**	Flow rate	~
	Temperature	**?**		Temperature	-
	Volume water	+		Volume water	~
	Nitrogen atmosphere	~		Nitrogen atmosphere	~
	Sodium citrate	+		Sodium citrate	-
	Sodium chloride	**?**		Sodium chloride	-
	Sodium citrate + Sodium chloride	+		Sodium citrate + Sodium chloride	-
Effect of characteristics on battery capacity			Effect of characteristics on DPSC cell viability		
Capacity	Diameter	-	**Cell viability**	Diameter	+
	Crystallite size	+		Crystallite size	**?**
	Fe(II)/Fe(III)	+		Fe(II)/Fe(III)	-
	Weight loss	**?**		Weight loss	**?**

In addition to viability and electrochemical performance, gene expression analysis was used to explore underlying cellular stress mechanisms. Although only limited and variable effects were observed, the consistent upregulation of the oxidative stress marker *HMOX1* at 100 µg/mL suggests that oxidative stress may contribute to toxicity. Notably, even PB-3, which showed no decrease in cell viability at this concentration, triggered a stress response at the gene expression level. Furthermore, shifts in mitochondrial dynamics genes (*MFF* and *MFN1*) were observed for smaller particles, indicating potential intracellular stress responses related to particle uptake. While the gene expression results do not fully explain the mechanisms behind the observed toxicity patterns, they provide initial clues and underscore the need for further mechanistic studies.

Overall, Prussian blue shows strong potential as a safe and sustainable cathode material for sodium-ion batteries. By carefully tuning its physicochemical properties, it is possible to optimize both safety and performance, advancing the development of environmentally friendly and safe energy storage technologies.

LIMITATIONS TOWARDS FUTURE APPLICATIONS

In this study, relatively high concentrations of Prussian blue particles were tested on dental pulp stem cells. Although these concentrations likely exceed realistic exposure levels, the results provide valuable insights into how particle characteristics influence both electrochemical performance and cellular toxicity. To assess the safety of these materials for specific applications, follow-up research is needed to investigate their release throughout the battery life cycle: during production, usage, and disposal. This will allow for the estimation of realistic exposure levels for different target groups, such as pregnant individuals or battery factory workers. Based on these insights, the most promising materials can be selected for further testing under more representative conditions. Once realistic exposure scenarios are established, toxicological assessment should be expanded by confirming results in other cell types (e.g., bone marrow-derived stem cells) or barrier models (e.g. intestinal, placental, or lung models), extending the exposure duration to study potential long-term effects, and evaluating toxicity during the differentiation of stem cells into various lineages, rather than focusing solely on undifferentiated cells as done in this study.

Electrochemical testing also has its limitations. Particle samples with a low Fe(II)/Fe(III) ratio showed the most promise in terms of reduced toxicity, making them attractive from a safety perspective. However, this lower ratio also means that less sodium is incorporated into the material during synthesis. While this benefits

biocompatibility, it reduces the amount of sodium available for cycling. In this study, electrochemical performance was evaluated in half-cell configurations, where the cathode is tested against a metallic sodium electrode that provides an excess of sodium ions. In contrast, real-world sodium-ion batteries use full-cell configurations, where the anode, typically made of hard carbon, contains no sodium initially (42). All available sodium must therefore come from the cathode. If the cathode contains too little sodium, the cell starts with a deficit, leading to poor initial capacity and limited cycling performance. Thus, while low-Fe(II)/Fe(III) materials show promise for reducing toxicity, their practical application in full cells may require additional strategies such as pre-sodiation to ensure sufficient sodium availability without compromising safety (43).

Acknowledgements – Reja Trippaers would like to thank Prof. Dr. An Hardy, Prof. Dr. Marlies K. Van Bael, Dr. Ir. Dries De Sloovere, Prof. Dr. Karen Smeets, and Prof. Dr. Nelly Seanen for welcoming her into their research groups and providing the opportunity to undertake this internship. Special appreciation goes to Dr. Ir. Dries De Sloovere and Prof. Dr. Nelly Seanen for their guidance in the lab, offering numerous opportunities to learn new techniques and work independently, as well as for their valuable input during the writing process. Anke Huysmans, Digvijay Ghogare, and the PhD candidates from the DESINe research group are warmly thanked for their analyses. Sander Stulens is gratefully acknowledged for his assistance with the atlas reactor. Finally, Anneleen Peeters, Lisa Reynders, and their supervisors Ines Tajeda and Anke Huysmans are sincerely thanked for their availability and support in the lab.

Author contributions – Prof. Dr. An Hardy, Prof. Dr. Marlies K. Van Bael, Dr. Ir. Dries De Sloovere, Prof. Dr. Karen Smeets, and Prof. Dr. Nelly Seanen conceived and designed the research. Reja Trippaers, Dr. Ir. Dries De Sloovere, and Prof. Dr. Nelly Seanen performed experiments and data analysis. Anke Huysmans provided TEM analyses. Digvijay Ghogare performed ICP-OES measurements. PhD candidates from the DESINe research group conducted XRD analyses. Reja Trippaers wrote the manuscript with guidance from Dr. Ir. Dries De Sloovere and Prof. Dr. Nelly Seanen. The text in this thesis was supported by GenAI.

REFERENCES

1. Hwang J-Y, Myung S-T, Sun Y-K. Sodium-ion batteries: present and future. Chemical Society Reviews. 2017;46(12):3529-614.
2. Kamble A, Walvekar A. A Review Paper on Comparison of Lithium and Sodium Ion Batteries for Electric Vehicle2024.
3. Wolters L, Brusselaers J. The energy transition paradox: How lithium extraction puts pressure on environment, society, and politics. The Extractive Industries and Society. 2024;19:101498.
4. EuropeanCommission. Lithium-based batteries supply chain challenges [Available from: https://rmis.jrc.ec.europa.eu/analysis-of-supply-chain-challenges-49b749.
5. EuropeanCommission. Critical raw materials.
6. Domingues AM, de Souza RG, Luiz JVR. Lifecycle social impacts of lithium-ion batteries: Consequences and future research agenda for a safe and just transition. Energy Research & Social Science. 2024;118:103756.
7. Lithium-ion batteries need to be greener and more ethical. Nature. 2021;595(7865):7-.
8. CAS. A Review of the Current Methods and Global Developments 2022 [Available from: https://www.cas.org/resources/cas-insights/lithium-ion-battery-recycling.
9. Mrozik W, Rajaeifar MA, Heidrich O, Christensen P. Environmental impacts, pollution sources and pathways of spent lithium-ion batteries. Energy & Environmental Science. 2021;14(12):6099-121.
10. You Y, Wu X-L, Yin Y-X, Guo Y-G. High-quality Prussian blue crystals as superior cathode materials for room-temperature sodium-ion batteries. Energy & Environmental Science. 2014;7(5):1643-7.
11. Kjeldgaard S, Dugulan I, Mamakhel A, Wagemaker M, Iversen BB, Bentien A. Strategies for synthesis of Prussian blue analogues. Royal Society Open Science. 2021;8(1):201779.
12. Qiao S, Dong S, Yuan L, Li T, Ma M, Wu Y, et al. Structure defects engineering in Prussian blue cathode materials for high-performance sodium-ion batteries. Journal of Alloys and Compounds. 2023;950:169903.
13. Bornamehr B, Presser V, Zarbin AJG, Yamauchi Y, Husmann S. Prussian blue and its analogues as functional template materials: control of derived structure compositions and morphologies. Journal of Materials Chemistry A. 2023;11(20):10473-92.
14. Dugershaw BB, Aengenheister L, Hansen SSK, Hougaard KS, Buerki-Thurnherr T. Recent insights on indirect mechanisms in developmental toxicity of nanomaterials. Particle and Fibre Toxicology. 2020;17(1):31.
15. Hougaard K, Hansen J, Jackson P, Kyjovska Z, Boisen AM, Yauk C, et al. Developmental toxicity of engineered nanomaterials. Toxicology Letters. 2016;258:S22-S3.
16. Aricò AS, Bruce P, Scrosati B, Tarascon J-M, van Schalkwijk W. Nanostructured materials for advanced energy conversion and storage devices. Nature Materials. 2005;4(5):366-77.
17. Huang YW, Cambre M, Lee HJ. The Toxicity of Nanoparticles Depends on Multiple Molecular and Physicochemical Mechanisms. Int J Mol Sci. 2017;18(12).
18. Adelizzi A, Giri A, Di Donfrancesco A, Boito S, Prigione A, Bottani E, et al. Fetal and obstetrics manifestations of mitochondrial diseases. J Transl Med. 2024;22(1):853.
19. Paunovic J, Vucevic D, Radosavljevic T, Mandić-Rajčević S, Pantic I. Iron-based nanoparticles and their potential toxicity: Focus on oxidative stress and apoptosis. Chem Biol Interact. 2020;316:108935.
20. Hu B, Cheng Z, Liang S. Advantages and prospects of stem cells in nanotoxicology. Chemosphere. 2022;291:132861.

21. Stefańska K, Volponi AA, Kulus M, Waśko J, Farzaneh M, Grzelak J, et al. Dental pulp stem cells – A basic research and future application in regenerative medicine. Biomedicine & Pharmacotherapy. 2024;178:116990.
22. Thanh NTK, Maclean N, Mahiddine S. Mechanisms of Nucleation and Growth of Nanoparticles in Solution. Chemical Reviews. 2014;114(15):7610-30.
23. Wang H, Zhu Q, Li H, Xie C, Zeng D. Tuning the Particle Size of Prussian Blue by a Dual Anion Source Method. Crystal Growth & Design. 2018;18(10):5780-9.
24. Zhao Y, Zhang J. Microstrain and Grain-Size Analysis From Diffraction Peak Width and Graphical Derivation of High-Pressure Thermomechanics. Journal of Applied Crystallography - J APPL CRYST. 2008;41:1108-.
25. Wang W, Gang Y, Hu Z, Yan Z, Li W, Li Y, et al. Reversible structural evolution of sodium-rich rhombohedral Prussian blue for sodium-ion batteries. Nature Communications. 2020;11(1):980.
26. Ojwang DO, Häggström L, Ericsson T, Ångström J, Brant WR. Influence of sodium content on the thermal behavior of low vacancy Prussian white cathode material. Dalton Transactions. 2020;49(11):3570-9.
27. Agnihotry SA, Singh P, Joshi AG, Singh DP, Sood KN, Shivaprasad SM. Electrodeposited Prussian blue films: Annealing effect. Electrochimica Acta. 2006;51(20):4291-301.
28. Li Z, Dadsetan M, Gao J, Zhang S, Cai L, Naseri A, et al. Revealing the Thermal Safety of Prussian Blue Cathode for Safer Nonaqueous Batteries. Advanced Energy Materials. 2021;11(42):2101764.
29. Bie X, Kubota K, Hosaka T, Chihara K, Komaba S. Synthesis and electrochemical properties of Na-rich Prussian blue analogues containing Mn, Fe, Co, and Fe for Na-ion batteries. Journal of Power Sources. 2018;378:322-30.
30. Che M, Jiang J, Yu J, Zhang R, Wu Z, Zhang Z, et al. Enhancing Sodium-Ion Storage Capacity and Stability in Metal–Organic Coordination Compounds by Bifunctional Coordinated Water Molecule. ENERGY & ENVIRONMENTAL MATERIALS. 2025;8(3):e12851.
31. Cheng M, Peng W, Hua P, Chen Z, Sheng J, Yang J, et al. In situ formation of pH-responsive Prussian blue for photoacoustic imaging and photothermal therapy of cancer. RSC Adv. 2017;7:18270-6.
32. Tournebize J, Sapin-Minet A, Bartosz G, Leroy P, Boudier A. Pitfalls of assays devoted to evaluation of oxidative stress induced by inorganic nanoparticles. Talanta. 2013;116:753-63.
33. He WL, Feng Y, Li XL, Wei YY, Yang XE. Availability and toxicity of Fe(II) and Fe(III) in Caco-2 cells. J Zhejiang Univ Sci B. 2008;9(9):707-12.
34. Auten RL, Davis JM. Oxygen Toxicity and Reactive Oxygen Species: The Devil Is in the Details. Pediatric Research. 2009;66(2):121-7.
35. Giese B, Klaessig F, Park B, Kaegi R, Steinfeldt M, Wigger H, et al. Risks, Release and Concentrations of Engineered Nanomaterial in the Environment. Scientific Reports. 2018;8(1):1565.
36. Gozzelino R, Jeney V, Soares MP. Mechanisms of cell protection by heme oxygenase-1. Annu Rev Pharmacol Toxicol. 2010;50:323-54.
37. Jang J, Park S, Choi IH. Increased Interleukin-11 and Stress-Related Gene Expression in Human Endothelial and Bronchial Epithelial Cells Exposed to Silver Nanoparticles. Biomolecules. 2021;11(2).

38. Hufnagel M, Schoch S, Wall J, Strauch BM, Hartwig A. Toxicity and Gene Expression Profiling of Copper- and Titanium-Based Nanoparticles Using Air–Liquid Interface Exposure. Chemical Research in Toxicology. 2020;33(5):1237-49.
39. Li Y, Wang W, Wu Q, Li Y, Tang M, Ye B, et al. Molecular control of TiO_2-NPs toxicity formation at predicted environmental relevant concentrations by Mn-SODs proteins. PLoS One. 2012;7(9):e44688.
40. Guo da D, Li Q, Tang HY, Su J, Bi HS. Zinc oxide nanoparticles inhibit expression of manganese superoxide dismutase via amplification of oxidative stress, in murine photoreceptor cells. Cell Prolif. 2016;49(3):386-94.
41. Youle RJ, van der Bliek AM. Mitochondrial Fission, Fusion, and Stress. Science. 2012;337(6098):1062-5.
42. Gao Y, Zhang H, Peng J, Li L, Xiao Y, Li L, et al. A 30-year overview of sodium-ion batteries. Carbon Energy. 2024;6(6):e464.
43. Hu J, Xu L, Li X, Liang Q, Ding C, Li Y, et al. Pre-sodiation strategies for constructing high-performance sodium-ion batteries. Journal of Materials Chemistry A. 2025;13(5):3206-35.

SUPPLEMENTARY INFORMATION

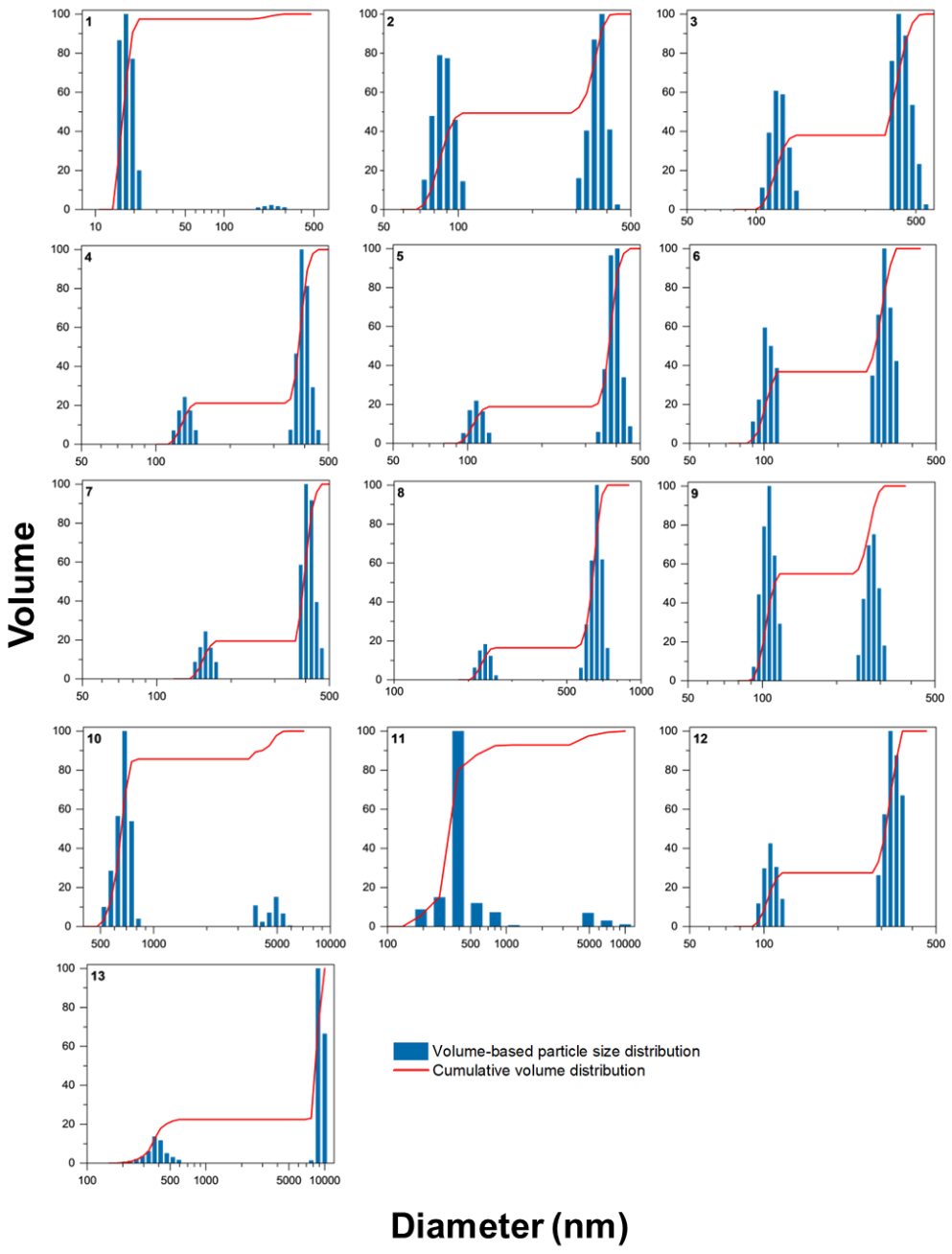

Fig. S1 – Hydrodynamic size distribution measured by DLS